https://doi.org/10.1016/j.apsusc.2019.06.109

Quantitative Investigation of Plasmonic Hot-Electron Injection by KPFM

Aoqun Jian[1], Kai Feng[1], Huaping Jia[1], Qianwu Zhang[2], Shengbo Sang[1*], and Xuming Zhang[3*]

1. MicroNano System Research Center, College of Information Engineering and Computer Science, Taiyuan University of Technology, Key Laboratory of Advanced Transducers and Intelligent Control System, Shanxi Province and Ministry of Education, Taiyuan University of Technology, Taiyuan 030000, China

2. Key Lab Specialty Fiber Opt & Opt Access Networks, Shanghai University, Shanghai 200072, China

3. Department of Applied Physics, Hong Kong Polytechnic University, Hong Kong 999077, China

1* Corresponding author E-mail: sunboa-sang@tyut.edu.cn
3* Corresponding author E-mail: apzhang@polyu.edu.hk

Graphical abstract

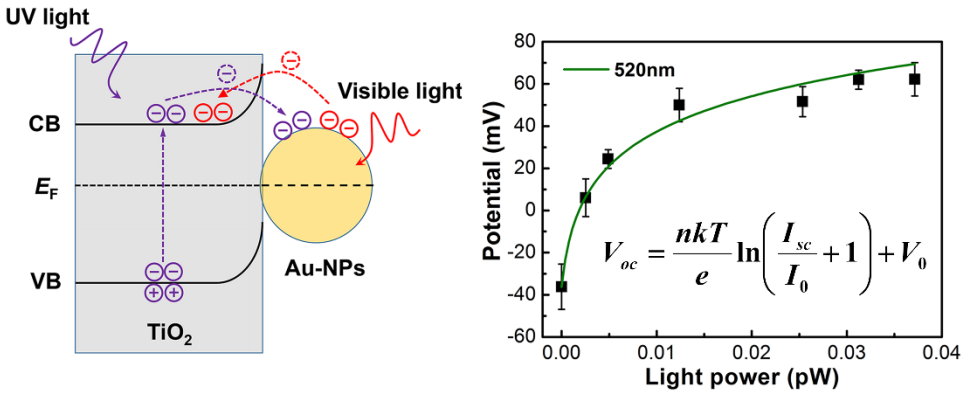

Abstract

Hot-electron injection is widely used in plasmonic devices. However, it is still lack of a direct theoretical model for performance prediction. This paper measures the surface potential of Au/TiO_2 film by Kelvin probe force microscope (KPFM) under various conditions, and then develops a theoretical model for quantitative interpretation. The model can well fit the relationship of surface potential versus light power under various irradiation wavelengths. The study in this paper opens the pathway for quantitative characterization of the efficiency of hot-electron injection and sheds light on improving the plasmonic efficiency of photoelectric conversion and photocatalysis.

Keywords hot-electron injection, Kelvin probe force microscope, surface potential, photocatalysis

1. Introduction

Hot-electron injection phenomenon is one of the hottest topics in surface science because of its crucial role in photoelectric energy conversion [1-15]. Although much research effort has been dedicated to making a variety of light-harvesting devices based on hot-electron injection, the overall efficiency of these devices is usually low [16], and the mechanism of hot-electron injection and its characteristics are still under intensive theoretical [17-19] and experimental study [16, 20-23]. Therefore, it is necessary to systematically examine the mechanism and to carefully quantify the influence factors of the efficiency. This will pave the way to the performance enhancement of plasmonic devices [24-26].

In previous studies, photoluminescence quenching [27], light-induced absorption spectroscopy and surface photoelectron spectroscopy [28] have been used to study the charge separation and transfer effect. These methods provide the basis for the study of charge dynamics but are limited to the low spatial resolution. On the other hand, Kelvin probe force microscope (KPFM) maps the surface potential to study the structural and electronic properties of functional surfaces and interfaces with a nanometer-scale spatial resolution [29-32]. It is a versatile imaging technique and has been applied to various materials/devices investigations, such as perovskite solar cells [33], photocatalysts [34] and nanoscale biomaterials [35]. Together with the corresponding AFM image of the same region of interest, KPFM imaging can be utilized for ultrasensitive label-free sensing. In this case, well-designed nanostructures (AuNPs and DNAs) act as nanoscale recognition elements to specifically capture the target analytes with tiny amount. Due to the high spatial resolution of KPFM/AFM images, these nanostructures can be identified easily by taking both of spatial and surface potential information into consideration. And the

concentrations of the target analytes can be found by measuring the surface potentials of the recognition-analyte complexes. High-sensitive detections of the metal cations (such as Al^{3+} [36], Hg^{2+} [37], Ag^{+} [38]) were achieved by using this method, and biomolecular interaction and binding affinities also can be observed at single molecule level [39]. Moreover, KPFM can be used to observe the charge transfer phenomena at the metal-semiconductor interface. For example, the surface potential of Au nanoparticles (AuNPs) on nonpolar ZnO [40] and TiO_2 nanotubes [41] under the UV irradiation were obtained by the KPFM. A new evidence supporting the charge transfer formation from the TiO_2 surface to the Au cluster was also demonstrated by KPFM [42].

In this paper, the surface potential of Au/TiO_2 under monochromatic light is measured by KPFM and a direct observation of the hot-electron injection is achieved. The variations of surface potential with respect to the incident light power and the irradiation wavelengths are investigated as well. For quantitative interpretation, a theoretical model is developed based on the classical theory of Schottky junction solar cells.

2. Experimental

2.1 Material Fabrication and Characterization

The schematic graph of the prepared sample is shown in **Fig. 1**(a). A thin TiO_2 film is formed on the ITO conductive glass in magnetron sputtering method. Then, Au NPs are deposited on the TiO_2 substrate by photochemical reduction. Weighing 30 μL $HAuCl_4$ aqueous solution with a concentration of 0.029 mol/L into a beaker containing 100ml of deionized water, subsequently, the magnetron sputtered TiO_2 film is placed at the bottom of the beaker and irradiated with xenon light source (NBeT, HSX-F300) for 5 minutes. After drying the sample, the Au NPs are deposited on the TiO_2 substrate. Scanning electron microscope (SEM, JEOL JSM-7100F) and noncontact mode atomic force microscope (AFM, Park systems NX10) are used to identify and characterize the Au/TiO_2 thin film. The absorbance spectra of samples are measured with the UV-VIS spectrophotometer (Shimadzu, UV-2600).

2.2 Surface Potential Measurements

The photo-induced surface potential changes of the samples are obtained with AFM in EFM mode at a scan rate of 0.25 Hz and the amplitude of 2 V by using a gold-coated silicon cantilever (PPP-NCSTAu, a force constant of 7.4 N/m and a resonance frequency of 160 kHz). The light coupled from a xenon light source by an optical fiber (SMA-905) illuminates on the sample at the incident angle of 45 degree. The KPFM measurements are all performed in a closed chamber for noise reduction. The wavelengths of the

incident light are adjusted by adopting specific filters (Throlabs, wavelength interval 20 nm) in the optical path.

3 Results and Discussion

Fig. 1(c) shows the morphology of the Au/TiO_2 film using the scanning electron microscopy. It can be found that AuNPs are sparsely distributed on the TiO_2 film surface (bright spots in **Fig. 1**(c), the related EDS result is shown in supplementary material S1), with the average diameter about 60 nm. The major physical processes in electrons transfer (Au/TiO_2 as an example) are depicted in **Fig. 1**(b). When the AuNPs are in direct contact with the n-type TiO_2 film, in order to achieve a consistent Fermi level, electrons diffuse from the TiO_2 side to Au and produce positively charged regions in the TiO_2 nanoparticles, forming a depletion region (space charge region). When the Au/TiO_2 film is irradiated by UV light, the photo-generated electrons in the TiO_2 region transfer into the Au particles due to a thermodynamic driving force so that the re-equilibration of the E_F levels of the TiO_2 and Au can be achieved. Under the irradiation of visible light, energetic hot-electrons are generated in the AuNPs due to the localized surface plasmon resonance (LSPR), most of which then migrate from the AuNPs to the conduction band of the TiO_2 film over the Schottky barrier at the Au/TiO_2 interface, and leave positively charged AuNPs at the same time.

Some qualitative experiments are carried out before the quantitative study. The surface potential images of Au/TiO_2 sample under UV or visible irradiation are plotted in **Fig. 2**(a)-(c) as measured by the KPFM, together with the corresponding AFM image of the same region of interest. In this method, the AFM tip scans over the surface to obtain the AFM topography image, at the same time an AC bias of frequency ω *via* a lock-in amplifier is applied to obtain the potential information. Therefore, the topographic image and the surface potential image are achieved simultaneously and correspond to each other spatially. Due to the obvious dimension differences between the AuNPs (about 60 nm) and TiO_2 particles (about 20 nm), these two kinds of particles are recognized firstly in the topographic image (the statistical distributions of particle sizes can be found in supplementary material **Fig. S3**) and their surface potentials are then obtained from the surface potential image. The dark and bright spots in **Fig. 2**(b) and 2(c) are attributed to the AuNPs after comparing with the AFM image in **Fig. 2**(a), showing that the surface potentials of AuNPs are lower than that of TiO_2 under UV light and become higher under visible light. This observation is consistent well with the charge transfer mechanism indicated in **Fig. 1**(b).

During the KPFM measurement, the light irradiation is kept constant onto the sample. Therefore,

the irradiation time is the same as the time of the KPFM measurement, which is typically 30 minutes for a single graph. On the other hand, the time of generation and transfer of hot electrons is very short (within the time scale of femtoseconds [2]). Therefore, the obtained surface potential differences indicate the steady-state concentration of hot electron near the surface of Au/TiO_2. It is a net effect of generation, separation, and recombination of carriers in the metal-semiconductors.

The origin of the steady state of surface potentials can be explained as follows: when the visible light is continually shone on the Au/TiO_2 film, hot electrons are generated in the AuNPs due to the LSPR effect and then migrate to the TiO_2 film, which forms a weak current (I_{sc}) flowing through the Schottky barrier at the Au/TiO_2 interface. As the hot electrons migrate and accumulate, an electric field is formed, whose direction is opposite to that of the current of hot electrons migration. As a result, a reverse current (I_d) is produced due to the built-in electric field. When this reverse current gradually grows and finally becomes equal to the hot-electron migration current, a stable potential difference is formed across the metal-semiconductor interface.

The transfer of electrons between AuNPs and TiO_2 film is more accurately studied under monochromatic irradiation by using narrow band-pass filters of visible light. The central wavelengths of six filters are 405 nm, 430 nm, 470 nm, 520 nm, 590 nm and 780 nm, which are characteristic wavelengths of the AuNPs absorption spectrum that correspond to the dip, the low absorption peak, the start of LSPR absorption, the LSPR peak, the end of LSPR absorption and the long wavelength side, respectively. The bandwidths of filters are all 20 nm, except for that of 780 nm (bandwidth 80 nm). For simplification, all these filters are referred to their central wavelengths in this paper.

The surface potential of the Au/TiO_2 sample is tested as a function of the incident light power under each filter (**Fig. 3**(a)-(c)). Here the value of surface potential is an average of ten prominent isolated AuNPs, and the error bar represents the standard deviation. Under 405 nm irradiation (*i.e.*, the dip of AuNP absorption), the surface potential presents a mild decrease with the increase of the light power that falls on each AuNP. This is because the little UV irradiation (395 – 400 nm) leaked from the blocking spectrum of the filter excites the electrons in the TiO_2 valence band to the conduction band, which then flow to the AuNPs. With the increase of light power, more electrons are excited and flow to the AuNPs, causing a decrease of the surface potential of AuNPs. Under 430 nm, similar trend can be observed due to the direct absorption by TiO_2 (see **Fig. 1**(d)). Under 470 nm (*i.e.*, the start of LSPR absorption), the potential increases very obviously but almost linearly. Under 520 nm (the LSPR peak) and the 590 nm

(the end of LSPR absorption), the trends are similar. The potential rises rapidly from -36 mV to +30 mV and then gradually saturates. However, the saturated value of 520 nm (about +62 mV) is larger than that of 590 nm (about +50 mV). Under 780 nm, the surface potential has very slight drop.

Due to the differences of individual AuNPs (e.g., morphologies and Au-TiO_2 contact states), the surface potentials of the analyzed individual AuNP are not exactly same with each other, which causes some slight fluctuations in the light-power *vs*. potential curves (e.g. the peak @0.031 pW for 405 nm irradiation, the peak @0.003 pW for 430 nm irradiation, the valley @0.031 pW for 470 nm irradiation, the valley @0.025 pW for 520 nm irradiation and the valley @0.058 pW for 780 nm irradiation). However, the general trends of surface potential due to the hot injection is still obvious since the change of surface potential (e.g., over 75 mV in Fig. 3(b)) is much larger than the fluctuations (here the most standard deviations of surface potentials are less than 15 mV). The observed trends and the measured date will be quantitatively explained using the theory below.

In the classical theory of Schottky junction solar cells, the characteristics of voltage V and current I at both ends of a solar cell are expressed by [43]:

$$I = I_d - I_{sc} = I_0\left[\exp\left(\frac{eV}{nkT}\right) - 1\right] - I_{sc} \tag{1}$$

where I_d is the diode current, I_0 is the reverse saturation current, I_{sc} is the short-circuit current, e is the electronic charge, n is a diode ideal factor, k is the Boltzmann constant, and T is the absolute temperature. When a Schottky junction solar cell is in an open circuit state, then it should have $I = 0$. Therefore, the current and the voltage follow the expression:

$$V_{oc} = \frac{nkT}{e}\ln\left(\frac{I_{sc}}{I_0} + 1\right) + V_0 \tag{2}$$

where V_{oc} is the open-circuit voltage and V_0 is the ground offset voltage of KPFM.

In our model, the hot-electron injected current acts as the short-circuit current I_{sc}. It rises from the hot electrons that are generated near the Au/TiO_2 interface by the plasmonic effect, and the relationship between the light power and the injected current $I_{photo\text{-}injection}$ can be written as:

$$I_{photo-injection} = I_{sc} = \frac{\lambda\eta F}{1240} = \frac{\lambda a_\lambda CF}{1240} \tag{3}$$

where η is the external quantum efficiency (EQE), λ is the wavelength of light, a_λ is the absorption coefficient of sample under different wavelengths of light, and C is the internal quantum efficiency (IQE). F is the light power irradiated on a single AuNP can be expressed by:

$$F = \frac{A}{S} F_0 \tag{4}$$

where F_0 is the power of output light, S and A are the areas of the light spot and the absorption cross-section of a single AuNP, respectively. To eliminate the size effect, the AuNPs with diameters around 60 nm are artificially selected and analyzed in the following experiments. The linear relationship between the current and the incident light power is also demonstrated by some other experiments [9, 10].

By substituting Eq. (3) into Eq. (2), the open-circuit voltage can be expressed by:

$$V_{oc} = \frac{nkT}{e} \ln\left[\frac{\lambda a_\lambda CF}{1240\, I_0} + 1\right] + V_0 \tag{5}$$

Here the reverse saturation current I_0 is given by:[44]

$$I_0 = AA^* T^2 \exp\left(-\frac{e\Delta\varphi_b}{kT}\right) \tag{6}$$

where A^* is the effective Richardson constant (1200 $A \cdot cm^{-2} \cdot K^{-2}$ for TiO_2), $\Delta\varphi_b$ is the barrier height of the Schottky junction.

According to Eq. (5), when the light power F is small enough (*i.e.*, $F \to 0$), it has $V_{oc}|_{F\to 0} = V_0$, that is, V_0 is equal to the voltage obtained in the dark environment. In Eq. (5), there are only three unknown parameters: n, $\Delta\varphi_b$ and C. Among them, n and $\Delta\varphi_b$ are only dependent on the temperature and the electronic properties of Au-TiO_2 Schottky junction, therefore they are independent of the wavelengths. In contrast, the parameter C is the unique parameter dependent on the wavelength.

As the hot-injection current in the Au-TiO_2 interface is dominated by the diffusion of majority carriers, the ideality factor n is close to 1. It is reported that $\Delta\varphi_b$ of Au-TiO_2 interface is in the range of 0.9 – 1.2 eV [8, 45-48]. In this study, we choose the middle value $\Delta\varphi_b$ = 1.05 eV. Therefore, the value of the internal quantum efficiency C can be determined by curve fitting of the experimental data as exemplified in **Fig. 4** (a)-(c). Since the hot-electron injection is a result of LSPR, the curve fitting focuses on mainly 470 nm, 520 nm and 590 nm. The results are listed in Table 1. Details of the curve fitting are described in supplementary material.

As stated above, the only wavelength-dependent parameter is C. According to the fitting results, the internal quantum efficiency C grows as the wavelength of light increases, whose trend is consistent well with theoretical prediction and the experimental data in recent study [21]. And the values of internal quantum efficiency C have the same order of magnitude, which is ~ 10^{-5}. This verifies the effectiveness of our model.

It is noted that Atwater et al. found the inappropriateness of the Fowler theory when the interband transition is present in addition to the intraband transition associated with the plasmonic resonance [21]. However, this cannot be confirmed in our experiment data due to the limited data points. A more detailed study will be conducted in future.

Next, the relationship between the saturated surface potential and the absorption spectrum is investigated. The five filters are used again for monochromatic illumination, and the light power is adjusted to be high enough to make sure the surface potential is always saturated for all five wavelengths. Seven AuNPs (labeled by A – G in **Fig. 5**(a)) are randomly chosen for further analysis. The KPFM measurement results are summarized and shown in **Fig. 5**(b). The average potential of these AuNPs grows gradually from the UV band to the visible band, reaches maximum point at 520 nm and then drops afterwards (Detailed trends of the potentials for selected Au NPs are plotted in **Fig. S5**). Similar conclusion also can be drawn from the fitting result above: 520 nm irradiation has the highest external quantum efficiency ($\eta = 1.08\times10^{-5}$) than the other two irradiations ($\eta = 3.29\times10^{-6}$ and 7.36×10^{-6} for 470 and 590 nm, respectively). It is also observed from **Fig. 5**(b) that the saturated surface potential follows the trend of the absorption spectrum of AuNPs (not that of Au/TiO_2 film). This is reasonable. According to Eq. (5), the open-circuit voltage V_{oc} increases with higher absorption coefficient a_λ. That is to say, the V_{oc} - λ curve should follow the same trend as the absorption spectrum. Such observation also agrees with the experimental results obtained by other groups by standardizing the photoelectric conversion efficiency [10, 49, 50]. This proves again the effectiveness of Eq. (5) and thus our model.

4. Conclusion

In this paper, the electron transfer of Au/TiO_2 irradiated by visible light of various monochromatic wavelengths is tested by using the KPFM, which are then interpreted by a theoretical model we proposed. Generally, the hot electrons in AuNPs are excited due to the LSPR effect, go over the Schottky barrier and eventually flow toward the TiO_2 film. When the irradiation wavelengths are within the LSPR peak of AuNPs, the surface potential varies with the incident light power in a similar trend: first a rapid increase and then a saturation state. Our model directly links the KPFM surface potential with the light power of single AuNP by combining the classical theory of Schottky junction solar cells and the reported hot-electron current expression. It can quantitatively describe the measured curves of surface potential versus light power under the irradiation of different wavelengths. It is also experimentally observed that

the saturated surface potential follows the absorption spectrum of the AuNPs. These findings above will provide a useful theoretical model for the design and development of plasmonics-based optoelectronic, photocatalytic and photosynthetic devices.

Acknowledgements

This study was financially supported by the National Natural Science Foundation of China (No. 61501316, 61471255, 61474079, 51622507 and 61377068), the Shanxi Scholarship Council of China (2015-047), 863 project (2015AA042601), Excellent Talents Technology Innovation Program of Shanxi Province (201805D211021), and Research Grants Council of Hong Kong (N_PolyU505/13, 152184/15E, 152127/17E and 152126/18E).

References

[1] P.V. Kamat, Photophysical, Photochemical and Photocatalytic Aspects of Metal Nanoparticles, J. Phys. Chem. 106 (2002) 7729-7744.

[2] S.M. Kim, S.W. Lee, S.Y. Moon, J.Y. Park, The effect of hot electrons and surface plasmons on heterogeneous catalysis, J. Phys. Condens. Matter. 28 (2016) 254002.

[3] A. Furube, L. Du, K. Hara, R. Katoh, M. Tachiya, Ultrafast plasmon-induced electron transfer from gold nanodots into TiO_2 nanoparticles, J. Am. Chem. Soc. 129 (2007) 14852-14853.

[4] M.W. Knight, H. Sobhani, P. Nordlander, N.J. Halas, Photodetection with active optical antennas, Science 332 (2011) 702-704.

[5] M.L. Brongersma, N.J. Halas, P. Nordlander, Plasmon-induced hot carrier science and technology, Nat. Nanotechnol. 10 (2015) 25-34.

[6] S. Linic, P. Christopher, D.B. Ingram, Plasmonic-metal nanostructures for efficient conversion of solar to chemical energy, Nat. Mater. 10 (2011) 911-921.

[7] I. Thomann, B.A. Pinaud, Z. Chen, B.M. Clemens, T.F. Jaramillo, M.L. Brongersma, Plasmon enhanced solar-to-fuel energy conversion, Nano Lett. 11 (2011) 3440-3446.

[8] S. Mubeen, G. Hernandez-Sosa, D. Moses, J. Lee, M. Moskovits, Plasmonic photosensitization of a wide band gap semiconductor: converting plasmons to charge carriers, Nano Lett. 11 (2011) 5548-5552.

[9] X. Zhang, Y.L. Chen, R.S. Liu, D.P. Tsai, Plasmonic photocatalysis, Rep. Prog. Phys. 76 (2013) 046401.

[10] Y. Nishijima, K. Ueno, Y. Yokota, K. Murakoshi, H. Misawa, Plasmon-Assisted Photocurrent Generation from Visible to Near-Infrared Wavelength Using a Au-Nanorods/TiO_2 Electrode, J. Phys. Chem. Lett. 1 (2010) 2031-2036.

[11] C. Tang, Z. He, W. Chen, S. Jia, J. Lou, D.V. Voronine, Quantum plasmonic hot-electron injection in lateral WSe_2/$MoSe_2$ heterostructures, Phys. Rev. B. 98 (2018).

[12] J.S. DuChene, G. Tagliabue, A.J. Welch, W.H. Cheng, H.A. Atwater, Hot Hole Collection and Photoelectrochemical CO_2 Reduction with Plasmonic Au/p-GaN Photocathodes, Nano Lett. 18 (2018) 2545-2550.

[13] M. Parente, S. Sheikholeslami, G.V. Naik, J.A. Dionne, A. Baldi, Equilibration of Photogenerated Charge Carriers in Plasmonic Core@Shell Nanoparticles, J. Phys. Chem. C. 122 (2018) 23631-23638.

[14] K. Wu, J. Chen, J.R. McBride, T. Lian, Efficient hot-electron transfer by a plasmon-induced interfacial charge-transfer transition, Science, 349 (2015).

[15] P. Narang, R. Sundararaman, H.A. Atwater, Plasmonic hot carrier dynamics in solid-state and chemical systems for energy conversion, Nanophotonics 5 (2016).

[16] D.C. Ratchford, A.D. Dunkelberger, I. Vurgaftman, J.C. Owrutsky, P.E. Pehrsson, Quantification of Efficient Plasmonic Hot-Electron Injection in Gold Nanoparticle-TiO_2 Films, Nano Lett. 17 (2017) 6047-6055.

[17] A.O. Govorov, H. Zhang, H.V. Demir, Y.K. Gun'ko, Photogeneration of hot plasmonic electrons with metal nanocrystals: Quantum description and potential applications, Nano Today 9 (2014) 85-101.

[18] R. Sundararaman, P. Narang, A.S. Jermyn, W.A. Goddard, 3rd, H.A. Atwater, Theoretical predictions for hot-carrier generation from surface plasmon decay, Nat. Commun. 5 (2014) 5788.

[19] M. Bernardi, J. Mustafa, J.B. Neaton, S.G. Louie, Theory and computation of hot carriers generated by surface plasmon polaritons in noble metals, Nat. Commun. 6 (2015) 7044.

[20] S. Tan, A. Argondizzo, J. Ren, L. Liu, J. Zhao, H. Petek, Plasmonic coupling at a metal/semiconductor interface, Nat. Photonics. 11 (2017) 806-812.

[21] G. Tagliabue, A.S. Jermyn, R. Sundararaman, A.J. Welch, J.S. DuChene, R. Pala, A.R. Davoyan, P. Narang, H.A. Atwater, Quantifying the role of surface plasmon excitation and hot carrier transport in plasmonic devices, Nat. Commun. 9 (2018) 3394.

[22] Y. Tian, T. Tatsuma, Mechanisms and applications of plasmon-induced charge separation at TiO_2 films loaded with gold nanoparticles, J. Am. Chem. Soc. 127 (2005) 7632-7637.

[23] W. Li, Z.J. Coppens, L.V. Besteiro, W. Wang, A.O. Govorov, J. Valentine, Circularly polarized light detection with hot electrons in chiral plasmonic metamaterials, Nat. Commun. 6 (2015) 8379.

[24] S. Mubeen, J. Lee, N. Singh, S. Kramer, G.D. Stucky, M. Moskovits, An autonomous photosynthetic device in which all charge carriers derive from surface plasmons, Nat. Nanotechnol. 8 (2013) 247-251.

[25] C. Clavero, Plasmon-induced hot-electron generation at nanoparticle/metal-oxide interfaces for photovoltaic and photocatalytic devices, Nat. Photonics. 8 (2014) 95-103.

[26] L. Zhou, D.F. Swearer, C. Zhang, H. Robatjazi, H. Zhao, L. Henderson, L. Dong, P. Christopher, E.A. Carter, P. Nordlander, N.J. Halas, Quantifying hot carrier and thermal contributions in plasmonic photocatalysis, Science 362 (2018) 69-72.

[27] A.E. Jailaubekov, A.P. Willard, J.R. Tritsch, W.L. Chan, N. Sai, R. Gearba, L.G. Kaake, K.J. Williams, K. Leung, P.J. Rossky, X.Y. Zhu, Hot charge-transfer excitons set the time limit for charge separation at donor/acceptor interfaces in organic photovoltaics, Nat. Mater. 12 (2013) 66-73.

[28] T. Yasuhiro, J.E. Moster, M. Grätzel, D.R. Klug, J.R. Durrant, Subpicosecond interfacial charge separation in dye-sensitized nanocrystalline titanium dioxide films. J. Phys. Chem. 100 (1996) 20056-20062.

[29] W. Melitz, J. Shen, A.C. Kummel, S. Lee, Kelvin probe force microscopy and its application, Surf. Sci. Rep. 66 (2011) 1-27.

[30] N. Adhikari, A. Dubey, D. Khatiwada, A.F. Mitul, Q. Wang, S. Venkatesan, A. Iefanova, J. Zai, X. Qian, M. Kumar, Q. Qiao, Interfacial Study To Suppress Charge Carrier Recombination for High Efficiency Perovskite Solar Cells, ACS Appl. Mater. Interfaces 7 (2015) 26445-26454.

[31] M.K. Siddiki, S. Venkatesan, D. Galipeau, Q. Qiao, Kelvin probe force microscopic imaging of the energy barrier and energetically favorable offset of interfaces in double-junction organic solar cells, ACS Appl. Mater. Interfaces 5 (2013) 1279-1286.

[32] S.-H. Lee, J.-S. Jo, J.H. Park, S.W. Lee, J.-W. Jang, A hot-electron-triggered catalytic oxidation reaction of plasmonic silver nanoparticles evidenced by surface potential mapping, J. Mater. Chem. A 6 (2018) 20939-20946.

[33] Z. Kang, H. Si, M. Shi, C. Xu, W. Fan, S. Ma, A. Kausar, Q. Liao, Z. Zhang, Y. Zhang, Kelvin probe force microscopy for perovskite solar cells, Sci. China Mater. 62 (2019) 776-789.

[34] R. Chen, F. Fan, T. Dittrich, C. Li, Imaging photogenerated charge carriers on surfaces and interfaces of photocatalysts with surface photovoltage microscopy, Chem. Soc. Rev. 47 (2018) 8238-8262.

[35] H. Lee, W. Lee, J.H. Lee, D.S. Yoon, Surface Potential Analysis of Nanoscale Biomaterials and Devices Using Kelvin Probe Force Microscopy, J. Nanomater. 2016 (2016) 1-21.

[36] W. Kim, G. Lee, M. Kim, J. Park, S. Jo, D.S. Yoon, Y.H. Park, J. Hong, J. Park, Al^{3+} ion sensing at

attomole level via surface-potential mapping of gold nanoparticle complexes, Sensors. Actuat. B-Chem. 255 (2018) 2179-2186.

[37] C. Park, K. Jang, S. Lee, J. You, S. Lee, H. Ha, K. Yun, J. Kim, H. Lee, J. Park, S. Na, A highly sensitive, direct and label-free technique for Hg^{2+} detection using Kelvin probe force microscopy, Nanotechnology 26 (2015) 305501.

[38] J. Park, S. Lee, K. Jang, S. Na, Ultra-sensitive direct detection of silver ions via Kelvin probe force microscopy, Biosens. Bioelectron. 60 (2014) 299-304.

[39] J. Park, J. Yang, G. Lee, C.Y. Lee, S. Na, S.W. Lee, S. Haam, Y.M. Huh, D.S. Yoon, K. Eom, T. Kwon, Single-molecule recognition of biomolecular interaction via Kelvin probe force microscopy, ACS Nano 5 (2011) 6981-6990.

[40] W.-H. Lin, J.-J. Wu, M.M.C. Chou, Y.-M. Chang, M. Yoshimura, Charge Transfer in Au Nanoparticle–Nonpolar ZnO Photocatalysts Illustrated by Surface-Potential-Derived Three-Dimensional Band Diagram, J. Phys. Chem. C. 118 (2014) 19814-19821.

[41] H. Yoo, C. Bae, Y. Yang, S. Lee, M. Kim, H. Kim, Y. Kim, H. Shin, Spatial charge separation in asymmetric structure of Au nanoparticle on TiO_2 nanotube by light-induced surface potential imaging, Nano Lett. 14 (2014) 4413-4417.

[42] H. Jing Chung, A. Yurtsever, Y. Sugimoto, M. Abe, S. Morita, Kelvin probe force microscopy characterization of TiO_2 (110)-supported Au clusters, Appl. Phys. Lett. 99 (2011) 123102.

[43] A.K. Ghosh, D.L. Morel, T. Feng, R.F. Shaw, C.A. Rowe, Photovoltaic and rectification properties of Al/Mg phthalocyanine/Ag Schottky−barrier cells, J. Appl. Phys. 45 (1974) 230-236.

[44] H. Altuntas, A. Bengi, U. Aydemir, T. Asar, S.S. Cetin, I. Kars, S. Altindal, S. Ozcelik, Electrical characterization of current conduction in Au/TiO_2/n-Si at wide temperature range, Mater. Sci. Semicond. Process. 12 (2009) 224-232.

[45] C. Ng, J.J. Cadusch, S. Dligatch, A. Roberts, T.J. Davis, P. Mulvaney, D.E. Gomez, Hot Carrier Extraction with Plasmonic Broadband Absorbers, ACS Nano 10 (2016) 4704-4711.

[46] J. Lee, S. Mubeen, X. Ji, G.D. Stucky, M. Moskovits, Plasmonic photoanodes for solar water splitting with visible light, Nano Lett. 12 (2012) 5014-5019.

[47] Y.K. Lee, C.H. Jung, J. Park, H. Seo, G.A. Somorjai, J.Y. Park, Surface plasmon-driven hot electron flow probed with metal-semiconductor nanodiodes, Nano Lett. 11 (2011) 4251-4255.

[48] N. Szydlo, R. Poirier, I - V and C - V characteristics of Au/TiO_2 Schottky diodes, J. Appl. Phys. 51 (1980) 3310-3312.

[49] L. Du, A. Furube, K. Hara, R. Katoh, M. Tachiya, Ultrafast plasmon induced electron injection mechanism in gold–TiO_2 nanoparticle system, J. Photoch. Photobio. A. 15 (2013) 21-30.

[50] K. Ueno, H. Misawa, Photochemical reaction fields with strong coupling between a photon and a molecule, J. Photoch. Photobio. A. 221 (2011) 130-137.

Figures

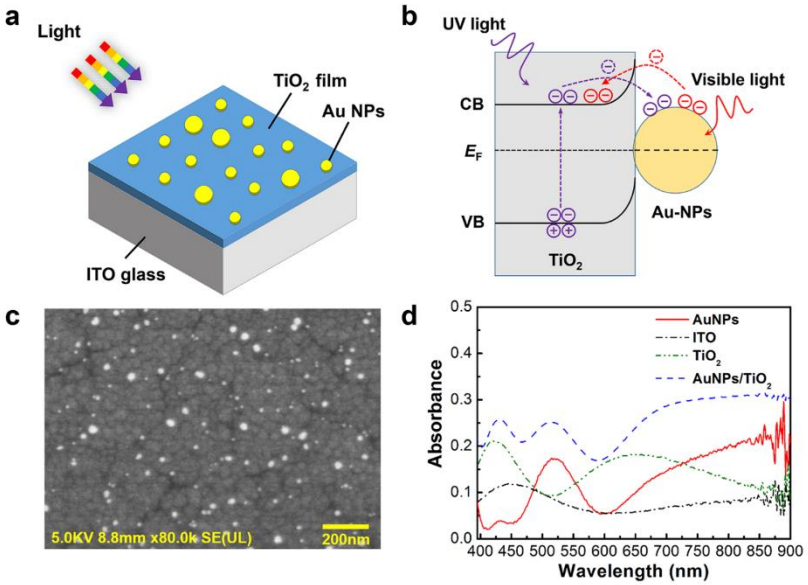

Fig. 1. (a) The schematic graph of the sample structure. From bottom to top, it consists of a TiO_2 film on the ITO glass substrate and a layer of Au nanoparticles (AuNPs) on the top. (b) The transfer of electrons between AuNPs and TiO_2 under the UV or visible irradiation. (c) The scanning electron micrograph of AuNPs on the TiO_2 surface. (d) The measured absorption spectra of different samples. The ITO film presents very low absorption with a peak at 450 nm (dash-dotted line). And the TiO_2 film has two absorption peaks at 420 and 650 nm (dash-dot-dotted line). The AuNPs themselves have an absorption peak at 520 nm with the bandwidth of 70 nm (solid line) due to the localized surface plasmon resonance (LSPR). After the AuNPs are deposited on the TiO_2 layer, it has also two absorption peaks at 430 and 520 nm (dashed line)

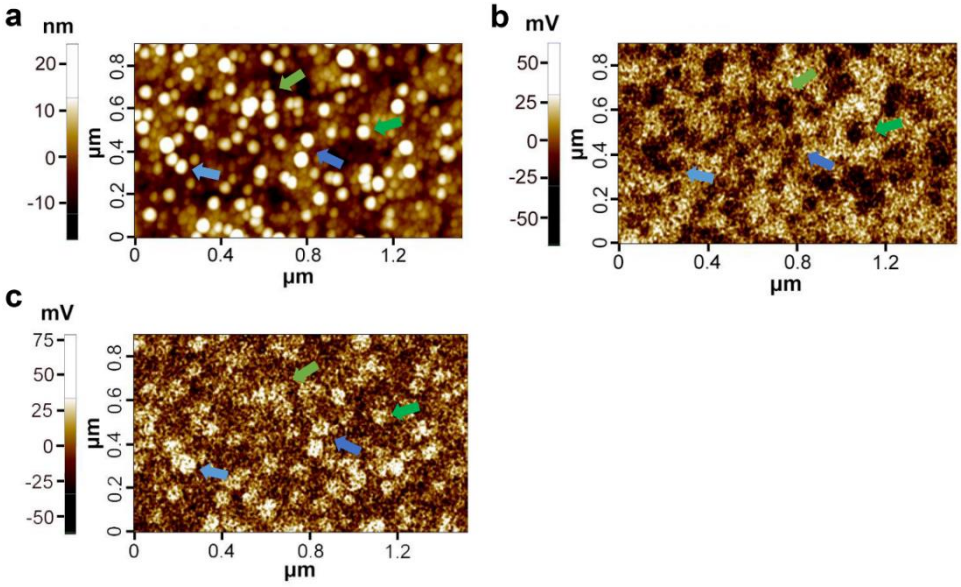

Fig. 2. The AFM topography (a) and the simultaneously obtained surface potential images of Au/TiO_2 under the UV (b) and the visible irradiation (c). The arrows with same color indicate the same particles in these three graphs.

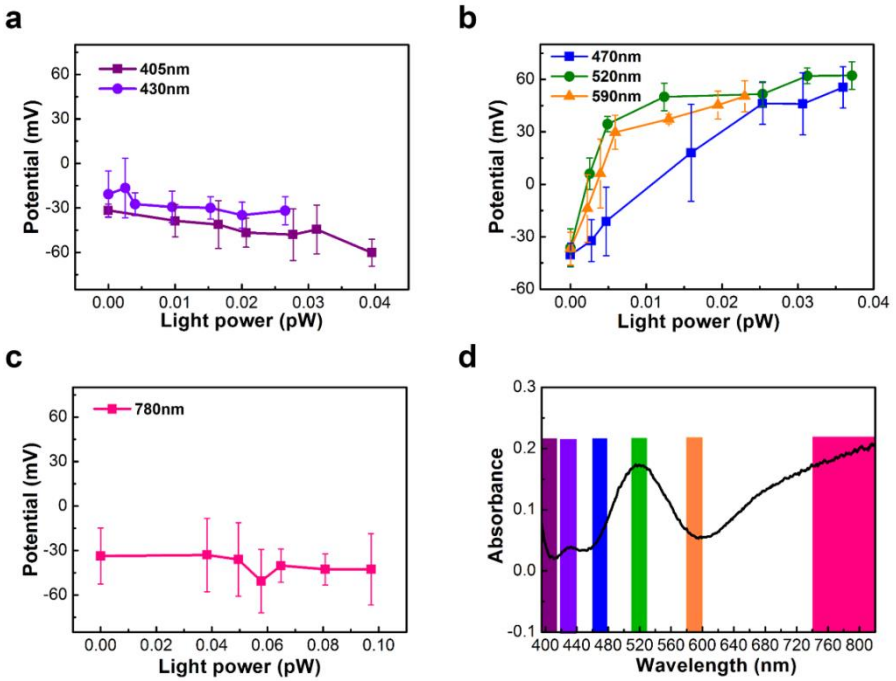

Fig. 3. The surface potential as a function of the light power under the irradiations of light at 405 nm and 430 nm (a), 470 nm, 520 nm and 590 nm (b), and 780 nm (c). The absorption spectrum of AuNPs and the positions of band-pass filters are plotted in (d).

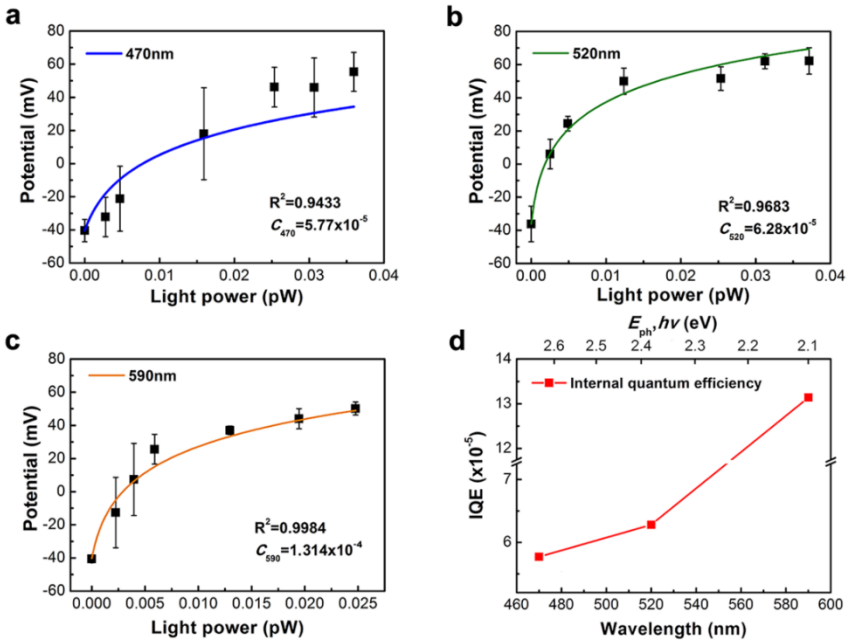

Fig. 4. Curve fitting of the surface potential as a function of light power using Eq. (5) when the irradiation wavelength is 470 nm (a), 520 nm (b), and 590 nm (c). The obtained internal quantum efficiency with respect to different irradiation wavelengths are summarized and plotted in (d).

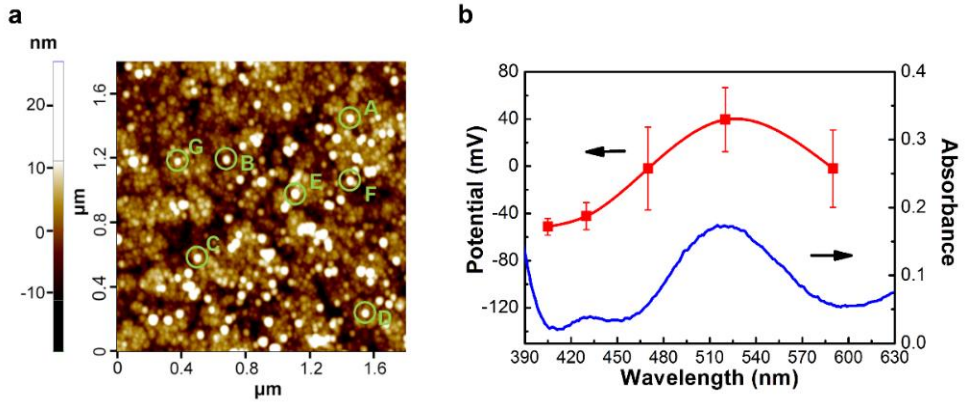

Fig. 5. Experimental study of the saturated surface potential with respect to the absorption spectrum of AuNPs. (a) Seven AuNPs (labeled by A – G) are randomly selected in the AFM image. (b) The absorption spectrum of AuNPs and the average potential change of these selected AuNPs under the irradiation of different wavelengths.

Table 1. The parameters of fitting curves in **Fig. 4** under the illuminations of different wavelengths.

Parameter	Symbols	Value		
		470 nm/2.64eV	**520 nm/2.38eV**	**590 nm/2.10eV**
Ideality factor	n		1	
Temperature	T		293 K	
Reverse sat. current	I_0		2.6×10^{-18} mA	
Barrier height	$\Delta\varphi_b$		1.05 eV	
IQE ($\times10^{-5}$)	C	5.77	6.28	13.14
EQE ($\times10^{-6}$)	η	3.29	10.80	7.36
Ground offset voltage	V_0	-40.4 mV	-36.2 mV	-40.2 mV